Carbon 179 (2021) 590–599

Contents lists available at ScienceDirect

Carbon

journal homepage: www.elsevier.com/locate/carbon

The influence of corrosion on diamond-like carbon topography and friction at the nanoscale

Fiona M. Elam [a, b], Feng-Chun Hsia [a, b], Stefan van Vliet [a], Roland Bliem [a, b], Liuquan Yang [c], Bart Weber [a, b], Steve E. Franklin [a, d, *]

[a] Advanced Research Center for Nanolithography (ARCNL), Science Park 106, 1098XG, Amsterdam, the Netherlands
[b] Van der Waals-Zeeman Institute, IoP, University of Amsterdam, Science Park 904, 1098XH, Amsterdam, the Netherlands
[c] School of Mechanical Engineering, The University of Leeds, Leeds, LS2 9JT, UK
[d] Department of Materials Science and Engineering, The University of Sheffield, Sheffield, S1 3JD, UK

ARTICLE INFO

Article history:
Received 4 February 2021
Received in revised form
6 April 2021
Accepted 19 April 2021
Available online 23 April 2021

Keywords:
Corrosion
Diamond-like carbon
Topography
Friction
Oxidation
Adhesion

ABSTRACT

The influence of corrosion upon the nanoscale topography and friction response of a hydrogenated amorphous carbon film (a-C:H) was investigated. Electrochemical atomic force microscopy was used to characterise topographical changes to the coating at two oxidative potentials. Corrosion of the coating at 1.5 V (corrosion rate 0.5 nm h^{-1}) resulted in no changes to the nanoscale topography; whereas corrosion at 2.5 V (corrosion rate 26.4 nm h^{-1}) caused the root mean square roughness of the a-C:H film topography to decrease, but the local fine-scale irregularity or 'jaggedness' of the surface to increase. X-ray photoelectron spectroscopy revealed that corrosion at both potentials oxidised the a-C:H surface to form alcohol, carbonyl and carboxyl groups. Lateral force microscopy and adhesion force measurements showed that both the friction force and surface adhesion of the coating increased upon corrosion. The outcome was attributed to the surface oxidation that had occurred at both oxidative potentials, resulting in several potential mechanisms including increased attractive intermolecular interactions and capillary forces. The highest friction coefficient was observed for the a-C:H film corroded at 2.5 V, and identified as a consequence of the jagged surface topography promoting an interlocking friction mechanism.

1. Introduction

Diamond-like carbon (DLC) is a class of thin film material that exists in several forms. Depending upon the synthesis method, DLC will contain different fractions of carbon-carbon sp^3, carbon-carbon sp^2, and carbon-hydrogen bonding; with its two major variants classified as tetrahedral hydrogen-free amorphous carbon (ta-C) and hydrogenated amorphous carbon (a-C:H) [1,2]. This chemical and structural versatility makes DLC a highly sought after material as a protective coating, owing to its many desirable properties including extreme mechanical hardness, excellent wear resistance, low friction coefficient, and high thermal and chemical stability [3,4]. DLC is currently utilised in applications within industries ranging from automotive to biomedical, and more recently in nanotechnology for use in micro-/nano-electromechanical systems (MEMS/NEMS) [2,4,5].

Many of these applications are required to function in humid and charged environments, meaning it is crucial that friction, wear and corrosion of the DLC coating are controlled [4]. Although DLC is widely reported as a corrosion resistant material [1,2,4–7], over sustained periods there remains potential for DLC to undergo corrosion (oxidation) at the surface, leading to changes in its nanoscale topography that could potentially impact eventual device performance. Several macro-scale studies have been undertaken to ascertain the tribological or tribo-corrosive behaviour of DLC upon immersion in corrosive media (typically simulated body fluid or NaCl solution), highlighting that DLC consistently outperformed various high-performance substrate materials in terms of a low friction and wear response [8–15]. However, upon investigation of the surface topography using scanning electron microscopy, evidence of micro-scale pitting was often reported after DLC coatings had undergone potentiodynamic polarisation measurements and immersion in different electrolytes [13,16–23]. Chlorine ions in the electrolyte solutions were identified as potential active species responsible for attacking DLC and inducing pitting corrosion via pinhole defects or nano-pores in the DLC film [11,16,22]. The amorphous nature of DLC should make it generally less prone

* Corresponding author. Advanced Research Center for Nanolithography (ARCNL), Science Park 106, 1098XG, Amsterdam, the Netherlands.
E-mail address: s.franklin@arcnl.nl (S.E. Franklin).

https://doi.org/10.1016/j.carbon.2021.04.068

to the formation of microscale fractures such as grain boundaries and pinhole defects [4]. However, studies have shown that the DLC deposition conditions, the coating thickness and the chosen substrate material can directly affect the microstructure of the DLC coating and its surface and interfacial roughness; properties which can then in turn influence corrosion resistance [4,7,19,23–25]. Promising DLC coatings with increased electrochemical resistance were found to have a high sp^3 content, few micro- or nanoscale defects such as pinholes, and a high degree of film uniformity [21,26].

Changes to the nature of the surface chemistry of DLC after potentiodynamic polarisation tests or immersion in various electrolytes were also investigated, most commonly utilising X-ray photoelectron spectroscopy (XPS) and Raman spectroscopy. Studies showed evidence for corrosion proceeding via a reduction in carbon sp^2 content [27], and the formation of oxides of C=O, C–OH, C–O and C(=O)–OH [15,17,27], indicating again that the carbon sp^3 fraction of DLC plays a key role in corrosion resistance [27]. Li et al. reported that the formation of C–O, C=O and C(=O)–O bonds on DLC surfaces sliding in H_2SO_4 lead to an increase in the interfacial shear strength, and thus also increased the friction coefficient of the tribological system [15]. There is a further claim that oxidation of DLC can increase the friction coefficient due to the intramolecular bond strength at the surface interface increasing; from the typically weak van der Waals interactions between DLC hydrocarbons (0.08 eV/bond), to stronger hydrogen bonding interactions (0.21 eV/bond) between C–O and C=O sites on the DLC, and water molecules [28–32], or polar surfaces.

The influence of corrosion on the nanoscale topography of a hydrogenated amorphous carbon film (a-C:H) and its subsequent influence upon the nanoscale friction response is as yet unexplored. These findings are likely to be of interest to the nanotechnology sector, in particular with regard to MEMS/NEMS applications. In this work, electrochemical atomic force microscopy (EC-AFM) is utilised: a technique that combines classical AFM using an unbiased probe together with a three electrode electrochemical cell to simultaneously corrode and map the a-C:H film surface topography evolution. The a-C:H film topographical changes are characterised statistically, and *ex situ* XPS and lateral force microscopy are used to examine the effect of corrosion on a-C:H film surface chemistry and friction at the nanoscale.

2. Experimental

2.1. Materials

The coating used in this study was a 480 nm thick hydrogenated amorphous carbon film (a-C:H) with the following properties: surface hardness ~20 GPa [33], Young's modulus ~210 GPa [33], hydrogen content ~36% [34], and density ~1.9 g cm^{-3} [2]. The film was deposited onto a pre-cut 35 × 35 mm^2 square of polished p-type single crystal (100) silicon wafer (University Wafer) (Fig. 1a). The coating was synthesised using plasma assisted chemical vapour deposition (PACVD) at 740 V pulsed DC bias with acetylene (BOC Ltd) as the precursor gas [33]. The PACVD process took place at 2.4 × 10^{-2} mbar and 200 °C, with a deposition time of 30 min. Samples were cleaned before and after corrosion using a deionised water, isopropanol (Sigma Aldrich), deionised water rinsing sequence, and stored under nitrogen.

2.2. Electrochemical, chemical and topographical investigations

All electrochemical and topographical experiments were carried out at room temperature (22 °C), inside a sound-proof chamber on a vibration isolation table. The a-C:H sample under investigation was mounted in an AFM-compatible electrochemical cell module (Bruker) (Fig. 1b), with the a-C:H-coated side making contact with two gold-coated pogo pins for the working electrode connection. The cell was placed in position inside the AFM (Dimension Icon, Bruker) (Fig. 1c), and the sample left to stabilise in a 2 ml electrolyte solution of 0.1 M KCl (Sigma Aldrich) for ~1 h. Open circuit potential (OCP) and chronoamperometry were performed with a bipotentiostat (CHI 760E, CH Instruments). An Ag|AgCl wire and Pt mesh acted as the reference and counter electrodes respectively, and the exposed sample surface was 5.81 cm^2. All potentials are referred *vs.* the Ag|AgCl (0.1 M KCl) reference electrode.

Prior to applying an anodic potential to corrode the a-C:H film, an OCP measurement was run for ~15 min until a stable voltage (±0.001 V) output was reached. Two anodic (oxidative) potentials were chosen to assess the influence of corrosion on a-C:H topography: 1.5 V and 2.5 V. Carbon is known to undergo oxidation at potentials above 1.0 V *vs.* standard hydrogen electrode (SHE) [35], (0.7 V *vs.* Ag|AgCl (0.1 M KCl). The chosen voltages were therefore within an appropriate range to assess the coating behaviour in mild conditions at 1.5 V towards more extreme corrosive conditions at 2.5 V. The oxidative potentials were applied to the samples for a total of 2.5 h in periods of 10, 20, 30 and 40 min as illustrated in Fig. 2. An *in situ* AFM micrograph was scanned at the interval between each corrosion time period. The measurement was implemented in peak force quantitative nanomechanical mapping (PF-QNM) mode, using a silicon 'ScanAsyst Fluid+' tip with a radius of ~2 nm. Images of 256 × 256 pixels were obtained with scanning areas of 1 × 1 μm^2 and 500 × 500 nm^2 at scan rates of 0.8 Hz and tapping forces of between 1.0 and 1.5 nN. Images were then processed using Gwyddion software in order to obtain cross-sectional height profiles and the height-height correlation function of each a-C:H coating as a function of corrosion time and condition [36].

Post-corrosion *ex situ* AFM micrographs (Dimension Icon, Bruker) were acquired of the a-C:H coating inside and outside the corroded regions, as indicated in Fig. 1d, using a silicon 'ScanAsyst Air' tip with a radius of ~2 nm. Images of 256 × 256 pixels were obtained with scanning areas of 1 × 1 μm^2 and 500 × 500 nm^2 at scan rates of 0.8 Hz, and processed as before.

To assess the influence of corrosion on the nanoscale friction response of the a-C:H film, lateral force microscopy (LFM) (Dimension Icon, Bruker) was similarly performed *ex situ* inside and outside the corroded regions of the coating (Fig. 1d) using two different probe types: a silicon 'RTESPA-300' tip with a radius of ~10 nm, spring constant k of ~57 N m^{-1} and deflection sensitivity S of 60.8 nm V^{-1}; and a silicon oxide colloidal probe with a diameter of 15 μm, k of ~2.8 N m^{-1} and S of 98.4 nm V^{-1} (Fig. 1e). The same two probes were used for all measurements. The normal force (cantilever deflection set-point) was varied by applying 200, 300, 400, 500 and 600 mV to the sharp probe; and 0, 200, 400, 600 and 800 mV to the colloidal probe. The set-point voltage is continuously compared to the vertical deflection signal of the photodiode in order to calculate the desired change in the Z piezo position required to maintain a constant cantilever deflection, and thus a constant normal force. Lateral force scans of 100 nm were acquired at 0.2 Hz (20 nm s^{-1}) for each applied normal force, with a density of 1024 samples/line for a total of four lines, each measured at a previously untouched location on the sample. The friction force was calculated from the resulting friction loops: averaging the difference between the trace and retrace values; and halving the result. To translate the lateral force signal (V) measured by the AFM photodiode into N, the wedge calibration method was used [37]. The probe was scanned 10 μm over a calibration sample (TGF11, MikroMasch) at a frequency of 0.1 Hz measuring 4096 data points per stroke, resulting in a conversion constant of ~0.056 mN V^{-1}. Force-displacement (*F-D*) measurements were performed using the

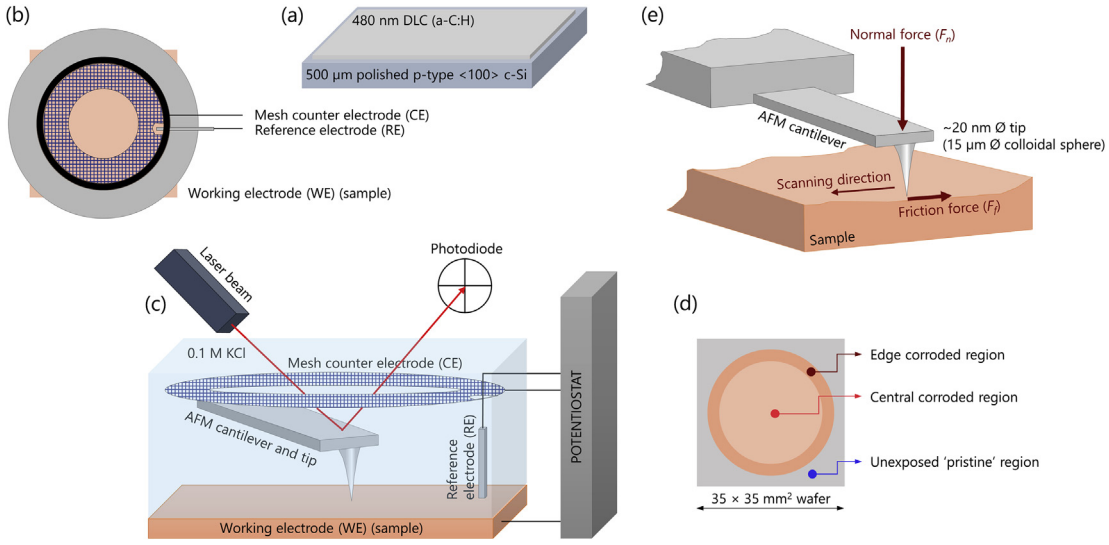

Fig. 1. Experimental and analytical schematics: (a) pristine a-C:H sample; (b) plan view of AFM-compatible electrochemical cell; (c) schematic of electrochemical-atomic force microscopy (EC-AFM) set-up; (d) post-corrosion regions of analysis; (e) lateral force microscopy (LFM) set-up. (A colour version of this figure can be viewed online.)

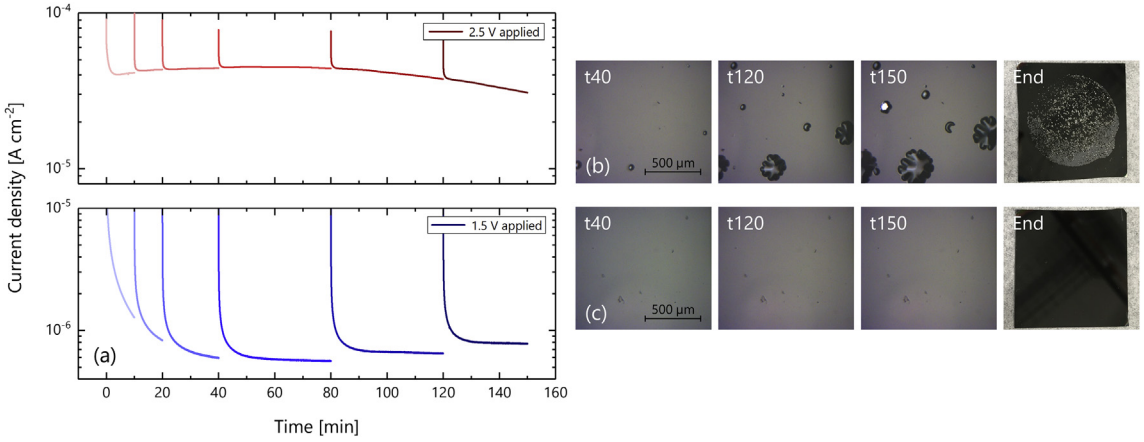

Fig. 2. Measured corrosion current density plotted as a function of time (a) when a potential of 2.5 V or 1.5 V is applied. Corresponding optical images of the a-C:H surface at time stamps of 40, 120 and 150 min, and final photographic image of the 35 × 35 mm^2 sample when: (b) 2.5 V is applied; (c) 1.5 V is applied. (A colour version of this figure can be viewed online.)

AFM in ramp mode to calculate the probe's spring constant, along with the surface adhesion at each of the studied locations. The normal force for each friction loop was calculated from the sum of the applied voltage to the probe and the adhesion force, taking into account any initial offset. The normal force was converted to nN by multiplying the force (V) with the probe spring constant k (nN nm^{-1}) and probe deflection sensitivity S (nm V^{-1}). To ensure the sharp probe did not wear as a result of the LFM study and thus influence the resulting friction force, the AFM tip radius was estimated using a tip reconstruction method [38]. The tip radius remained at ~10 nm after all measurements.

In order to determine the influence of corrosion on the chemical composition of the a-C:H surface, X-ray photoelectron spectroscopy (XPS) was performed (HiPP-3 Analyzer (entrance slit 2.5 mm), Scienta Omicron) on pristine and corroded samples. The measurements were carried out using a monochromatic Al K_α X-ray source operating at 14 kV with a 20 mA emission current. The system base pressure was ~2 × 10^{-9} mbar, and operating pressure ~5 × 10^{-9} mbar. Low and high-resolution spectra were acquired at pass energies of 300 eV and 100 eV respectively. The resulting spectra were processed and analysed using KolXPD software (Kolibrik). Fitting parameters are displayed in Table S1. For the lower resolution spectra acquired at a pass energy of 300 eV, no correction was performed with regard to the small variations that could arise from the differences in probing depth at the characteristic kinetic energies of the C 1*s* and Cl 2*p* region compared to the O 1*s* region.

3. Results and discussion

The initial open circuit potentials for the samples studied before undergoing corrosion fell within the range 0.186–0.170 V. Fig. 2 shows the measured corrosion current density evolution of the a-C:H film as a function of time, for the two studied oxidative potentials. The maximum stabilised corrosion current density for the sample corroded at 2.5 V was 4.48 × 10^{-5} A cm^{-2}, and for the sample corroded at 1.5 V, a significantly lower density of 7.89 × 10^{-7} A cm^{-2} was obtained. This difference in corrosion current density was reflected in the values calculated for the rate of corrosion CR (nm h^{-1}), using Equation (1) [39],

$$CR = \frac{Mj_{corr}}{\rho zF} \cdot K \quad (1)$$

where M is the molar mass (12 g mol^{-1}), j_{corr} is the corrosion current density (A cm^{-2}), ρ is the material density (1.9 g cm^{-3}), z is the number of electrons that participate in the chemical reaction (4 e^-, *vide infra*), F is the Faraday constant (C mol^{-1}) and K is a conversion factor (3.6×10^{10}) to nm h^{-1}. For simplicity, the parameters are based on the assumption that only the a-C:H coating is corroding, although it is possible in the case of the sample corroded at 2.5 V that the exposed Si wafer substrate was also oxidised. The corresponding values for the samples that underwent corrosion at 2.5 V and 1.5 V were 26.4 nm h^{-1} and 0.5 nm h^{-1} respectively. This stark difference in corrosion rate was also reflected in the optical appearance of the films as the corrosion time progressed. Fig. 2b illustrates the progression of the a-C:H coating corrosion at 2.5 V, showing ongoing pitting of the coating until the underlying Si wafer is exposed at 150 min. The pitting corrosion is liable to originate at a defect, pinhole or open pore within the coating network, providing an accelerated reaction pathway for the electrolyte to reach the underlying substrate, leading to an eventual deterioration in interface adhesion (Fig. S1) [23–25]. The gradual exposure of the Si substrate appears to be reflected in the measured corrosion current density progression with time. The values reach a maximum at approximately 60 min, after which the corrosion current begins to fall. This trend is considered to be in line with gradual passivation of the exposed Si wafer. The final image in Fig. 2b also highlights that the corrosion of the coating was somewhat non-uniform, related most probably to the EC cell geometry. For this reason it was decided to analyse an additional edge region of the coating in the post-analysis (Fig. 1d), where the influence of corrosion upon the a-C:H film was expected to be greater. In contrast, the sample corroded at 1.5 V shows no evidence of pitting or coating removal (Fig. 2c). This inert behaviour is reflected in the measured corrosion current density and rate.

As the chronoamperometry was performed using EC-AFM, micrographs at specific time intervals were obtained to illustrate the a-C:H surface topography evolution over the course of the corrosion experiment (Fig. S2). However, due to the *in situ* nature of the measurement, the AFM micrographs show some level of contamination from small particles potentially re-depositing on the surface. In order to perform an in depth statistical analysis into the influence of corrosion on the underlying a-C:H topography, additional *ex situ* AFM micrographs were obtained, ensuring as far as possible, no particles were present in any of the images. Hence, Fig. 3 shows examples of the typical *ex situ* post-corrosion AFM micrographs acquired at three different locations (Fig. 1d) on a-C:H samples corroded at 1.5 V (Fig. 3a–c) and 2.5 V (Fig. 3d–f). The pristine topography on first glance appears very similar to AFM micrographs of PACVD-synthesised a-C:H films reported elsewhere [40,41]. There is a clear similarity in the surface topographies of all micrographs where the a-C:H film was corroded at 1.5 V. This indicates that at this potential, the effect upon the surface structure of the a-C:H coating is negligible, which is also reflected in the very low corrosion rate (0.5 nm h^{-1}). However in contrast, there appears to be a distinct difference in surface topography between the pristine sample, and the centre and edge regions of the a-C:H film corroded at 2.5 V. Suggested also by the higher corrosion rate (26.4 nm h^{-1}), it appears that material removal has occurred across the whole of the a-C:H surface, and is not limited to defects points. The extent of material loss is also greater for the edge region of the coating, consistent with the observations made in relation to Fig. 2b, which indicated that the effect of corrosion would be more pronounced in this area. Therefore, not only does the 2.5 V anodic potential induce pitting of the a-C:H coating, it also results in a relatively uniform nanoscale surface material loss.

In order to quantify the information contained in Fig. 3, the height-height correlation function (HHCF), expressed as $H(\mathbf{r}) = [h(\mathbf{x}) - h(\mathbf{x}+\mathbf{r})]^2$, where $h(\mathbf{x})$ defines the surface height at in-plane positional vector $\mathbf{x}$, and $\mathbf{r}$ is a displacement vector [42], was plotted for each AFM micrograph (Fig. 4a and b). The HHCF thereby describes the average height difference between any two points separated by distance r. For a self-affine roughness, the HHCF follows the scaling behaviour below, enabling the extraction of three roughness parameters,

$$H(r) = \begin{cases} \propto r^{2\alpha}, & r \ll \xi \\ 2\sigma^2, & r \gg \xi \end{cases} \quad (2)$$

where α is the roughness exponent (the local irregularity of the surface), ξ is the lateral correlation length (the largest distance beyond which the surface height is not correlated), and σ is the root-mean-square (RMS) roughness [43]. The height-height correlation is plotted in a log-log scale to enable the slope in the region $r \ll \xi$ to be equal to 2α. The roughness exponent α has a value between 0 and 1; with values of α ($\approx$0) representing extremely jagged surfaces, and larger values ($\approx$1) signifying smooth peaks and troughs. The saturation plateau at $r \gg \xi$ provides the RMS roughness amplitude σ, according to the relation $H(r) = 2\sigma^2$, and the turning point determines the lateral correlation length ξ [43]. Hence the surface topography can be completely characterised by these three roughness parameters.

Fig. 4c and d illustrates the values calculated for the roughness parameters at three different locations (Fig. 1d) on the a-C:H samples corroded at 1.5 V and 2.5 V. In terms of the starting RMS roughness (σ) for both pristine samples, there appears to be a slight discrepancy, possibly due to minor sample-to-sample variation induced by the nature of the deposition process. Nevertheless, the analysis clearly confirms that corrosion at 1.5 V has little to no effect upon the surface topography of the a-C:H coating, which is evident from the absence of any significant difference in the roughness parameters calculated, regardless of measured location. Also verified is the finding that applying a potential of 2.5 V does indeed induce substantial changes to the a-C:H topography. Fig. 4d demonstrates the significant differences between the roughness parameters calculated at each location, and the progressive development in nature of the surface topography from the pristine a-C:H film, to the corroded centre and edge regions. The cross-sectional height profiles depicted in Fig. 4e and f effectively substantiate these findings; most notably with regard to the observation that the a-C:H coating shows an increase in the surface jaggedness (denoted by a decrease in α), an increase in the lateral distance whereby the surface height remains correlated (an increase in ξ), and a decrease in σ (the RMS roughness) upon corrosion at 2.5 V. Compared to the pristine a-C:H surface, the 2.5 V corroded surface has therefore increased in roughness at a short spatial scale and decreased in roughness at a longer spatial scale [44].

To establish qualitatively if corrosion of the a-C:H film also altered the chemical composition of the surface, X-ray photoelectron spectroscopy (XPS) was performed on the pristine a-C:H coating, and the central regions of samples corroded at 1.5 V and 2.5 V (Table 1 and Fig. 5), with detailed atomic percentages shown in Table S2. The spectra clearly show that oxidation has taken place on the surface of both corroded samples [15,17,27], with evidence of the formation of alcohol (C–OH), carbonyl (C=O) and carboxyl groups (C(=O)–OH) apparent at the higher binding energy of the C 1*s* shoulder [45–47]. Moreover, the difference in oxidation extent

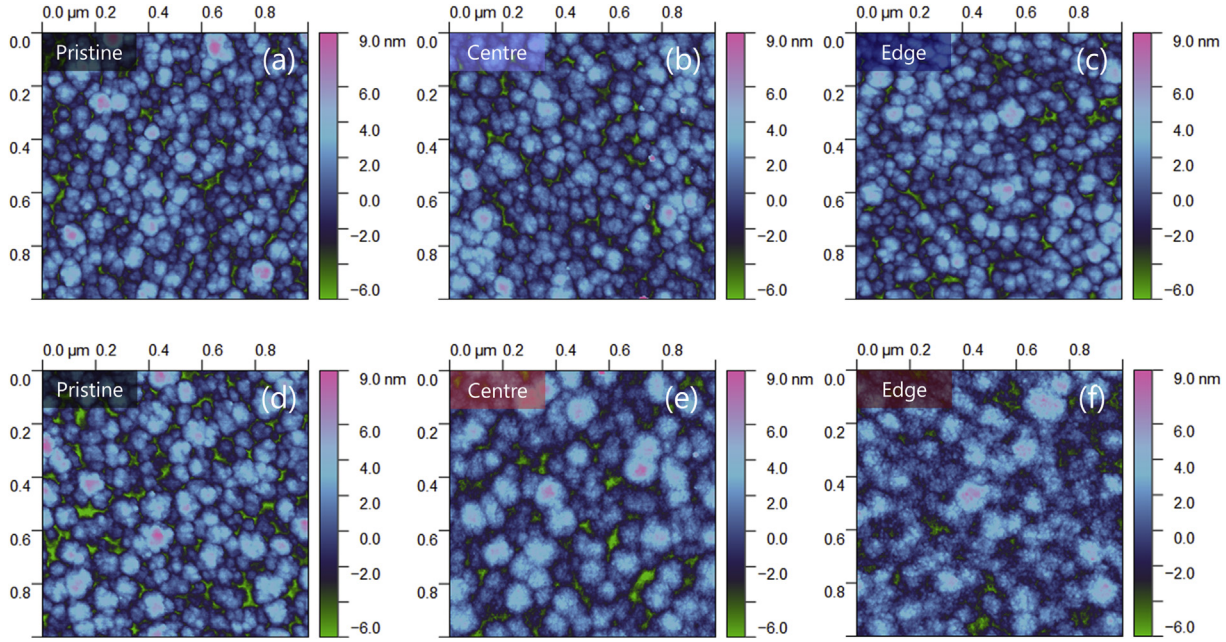

Fig. 3. AFM micrographs with scanning areas of 1 × 1 µm^2 illustrating the typical surface topography evolution of a-C:H at various coating and corrosion locations (Fig. 1d) when: (a)–(c) 1.5 V is applied; (d)–(f) 2.5 V is applied. (A colour version of this figure can be viewed online.)

between the pristine and corroded samples is likely greater than the values reported, due to a probable contribution from the high binding energy asymmetric tail of the C sp^2 peak. This tail artificially enhances the apparent intensity of all oxygen containing species, and is expected to contribute significantly to the observed peak intensities for the pristine a-C:H film in this region.

A subtle reduction in the sp^2 contribution of the main C 1*s* peak at ~284.5 eV can also be observed for both corroded samples, evident from the sp^2:sp^3 ratios displayed in Table 1. Possible reaction pathways for the oxidation of carbon sp^2 bonds in a-C:H are presented in Fig. S3. There is also evidence to suggest carbon dioxide formation; particularly in the case of the a-C:H film corroded at 2.5 V, where conditions are suitable for CO_2 evolution according to the Pourbaix diagram of carbon [48]. The formation of CO_2 (O=C=O) is the final oxidation step in the oxidation pathway of a carbon sp^2 bond after the formation of carboxyl groups (Fig. S3); and since it is a leaving product, it is therefore undetectable using this spectroscopic technique. However, the AFM micrographs in Fig. 3e and f, which seem to depict nanoscale surface material loss; and similarly the measured corrosion current that resulted in a calculated corrosion rate of 26.4 nm h^{-1}, provide an indication to the formation of leaving products such as CO_2. This finding also justifies the chosen value of 4 e^- for Equation (1), according to $C + 2H_2O \rightarrow CO_2 + 4H^+ + 4e^-$, $E^0 = 0.207$ V *vs.* SHE [35,48,49].

The similarities in the oxidation extent of both corroded samples regardless of the applied potential is also noteworthy. In the absence of pitting it is understood that an interplay exists between passivation (i.e. the stable formation of a thin film of oxidised carbon species that blocks the surface from oxidation), and the breakdown of that surface oxide film at higher oxidative potentials leading to material removal. It is expected that a-C:H passivation occurs on a relatively short time scale, but that the protective layer is not everlasting, and thus a-C:H will undergo material removal as is observed when corrosion at 2.5 V takes place.

Lastly, to ascertain the influence of corrosion upon the nanoscale friction behaviour of the a-C:H coating, LFM using a Si probe with a ~10 nm radius was performed at various coating and corrosion locations (Fig. 1d and e), in addition to force-displacement measurements to determine the surface adhesion response (Fig. 6). Evident in all cases, is the finding that the corroded surface exhibits a higher adhesion force than the pristine a-C:H coating (Fig. 6a). This can be attributed to capillary adhesion and stronger attractive interfacial dipole-dipole interactions (van der Waals interactions and hydrogen bonding (H-bonding)) acting upon the Si probe [28–32]. The Si probe has a native oxide layer, terminated with silanol groups (-Si-O-H), that are attracted to the electronegative oxygen atoms found in the oxidation products (C–O–H, C=O and C(=O)–O–H) on the corroded a-C:H surface (Table 1, Fig. 5). These oxidation products also make the surface more hydrophilic [50], implying a lower water contact angle and higher surface free energy. This facilitates the growth and volume of water contributing to the capillary bridge between the Si probe and a-C:H surface, thereby increasing the capillary force and thus the adhesion force [31,32,51–53]. Capillary forces have been shown in most cases to contribute to a greater extent than van der Waals interactions towards the adhesion force for systems measured in air [31,51,52]. Capillary adhesion can also be influenced by the surface topography of the contacts, which affects the interfacial separation, thus changing the area of contact over which the capillary adhesion can act [54]. However, in this case, no significant difference is observed between the measured adhesion forces for the 1.5 V and 2.5 V corroded a-C:H samples, which have very similar surface chemistry but different surface topographies. This is attributed to the ~10 nm radius of the sharp Si probe, which dominates the geometry of the contact interface in the normal direction for all samples (Fig. S4), whereby the observed differences in a-C:H surface roughness become irrelevant. Overall, it is clear that the surface oxidation products and thus the surface chemistry of the corroded a-C:H film is responsible for the increased adhesion force.

Fig. 6b shows the friction response, measured using LFM, of the a-C:H coatings as a function of the normal force F_N, where the latter incorporates the adhesion force values displayed in Fig. 6a. The friction coefficient μ, was calculated using the relationship $F_f = \mu F_N$, where F_f is the measured friction force. The friction force, and

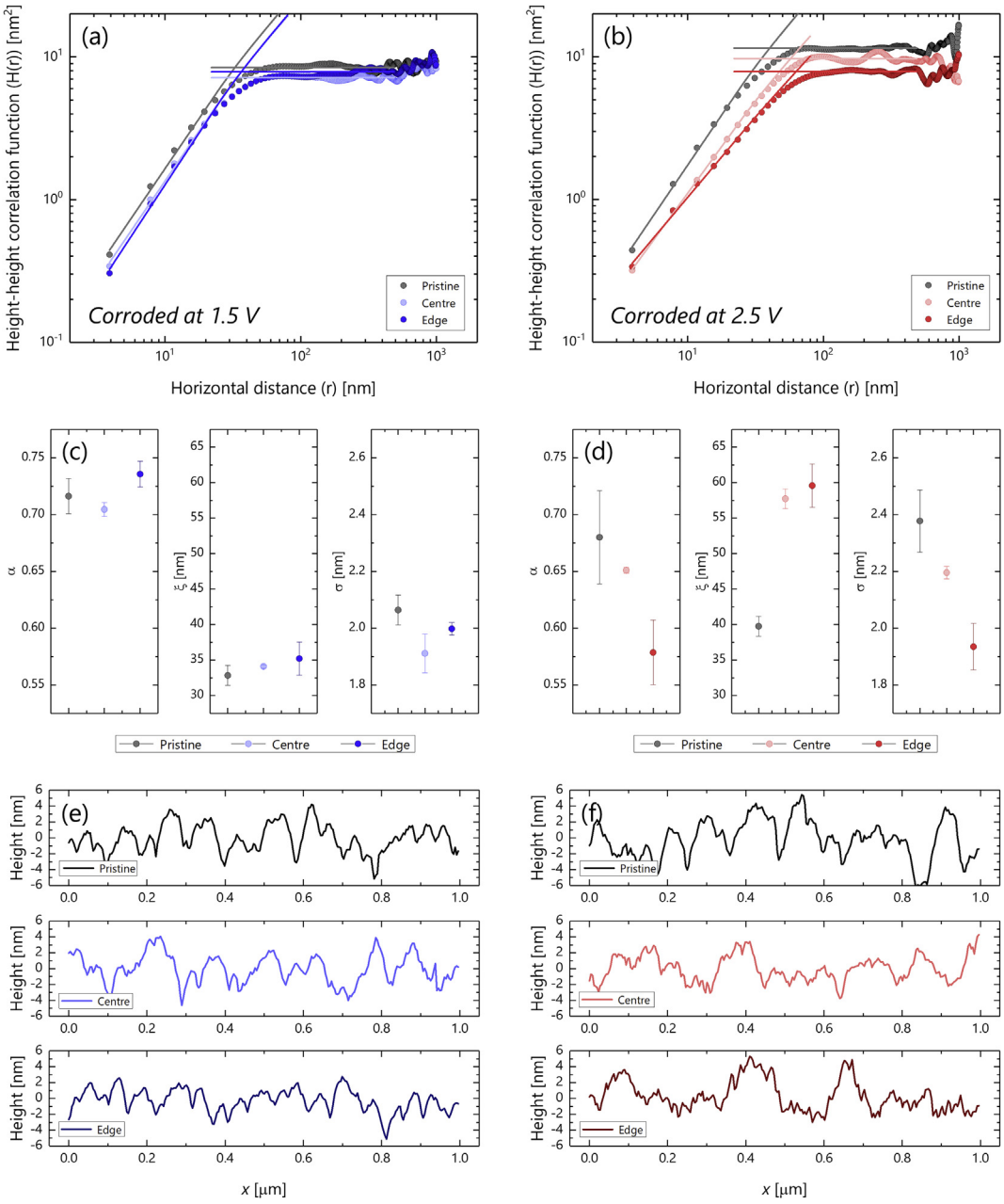

Fig. 4. Topographic data obtained from AFM micrographs (Fig. 3) of a-C:H at various coating and corrosion locations (Fig. 1d): Height-height correlation function (HHCF) of a-C:H coatings plotted as a function of horizontal distance, corroded at (a) 1.5 V and (b) 2.5 V; roughness statistical parameters calculated from HHCF for a-C:H coatings corroded at (c) 1.5 V and (d) 2.5 V (each data point based on values from three discrete AFM micrographs); typical cross-sectional height profiles for a-C:H coatings corroded at (e) 1.5 V and (f) 2.5 V. (A colour version of this figure can be viewed online.)

Table 1
XPS compositional analysis for pristine and corroded a-C:H films. Atomic percentages calculated from spectra acquired at pass energy (PE) of 300 eV. Ratio comparison with respect to C sp^2 calculated from deconvolution of spectra acquired at pass energy 100 eV (Fig. 5).

Coating	Atomic percentage (PE300)			Ratio comparison with respect to C sp^2 (PE100)					
	C [%]	O [%]	Cl [%]	C sp^2	C sp^3	C–O[a]	C=O[a]	O–C=O[a]	C–Cl[a]
Pristine a-C:H	93.4	6.6	0.0	1.000	0.308	0.070	0.022	0.012	0.000
1.5 V Corroded a-C:H	87.7	11.3	1.1	1.000	0.328	0.072	0.054	0.042	0.019
2.5 V Corroded a-C:H	86.3	12.4	1.3	1.000	0.316	0.074	0.053	0.047	0.021

[a] Probable contribution from high binding energy asymmetric tail of C sp^2 peak, with greatest influence likely on C–O values calculated for the pristine a-C:H sample.

thus the friction coefficient (the gradient of the linear fit in Fig. 6b) is clearly seen to increase as a function of corrosion extent, with the a-C:H film corroded at 2.5 V exhibiting the highest friction coefficient and both pristine a-C:H coatings demonstrating equally low

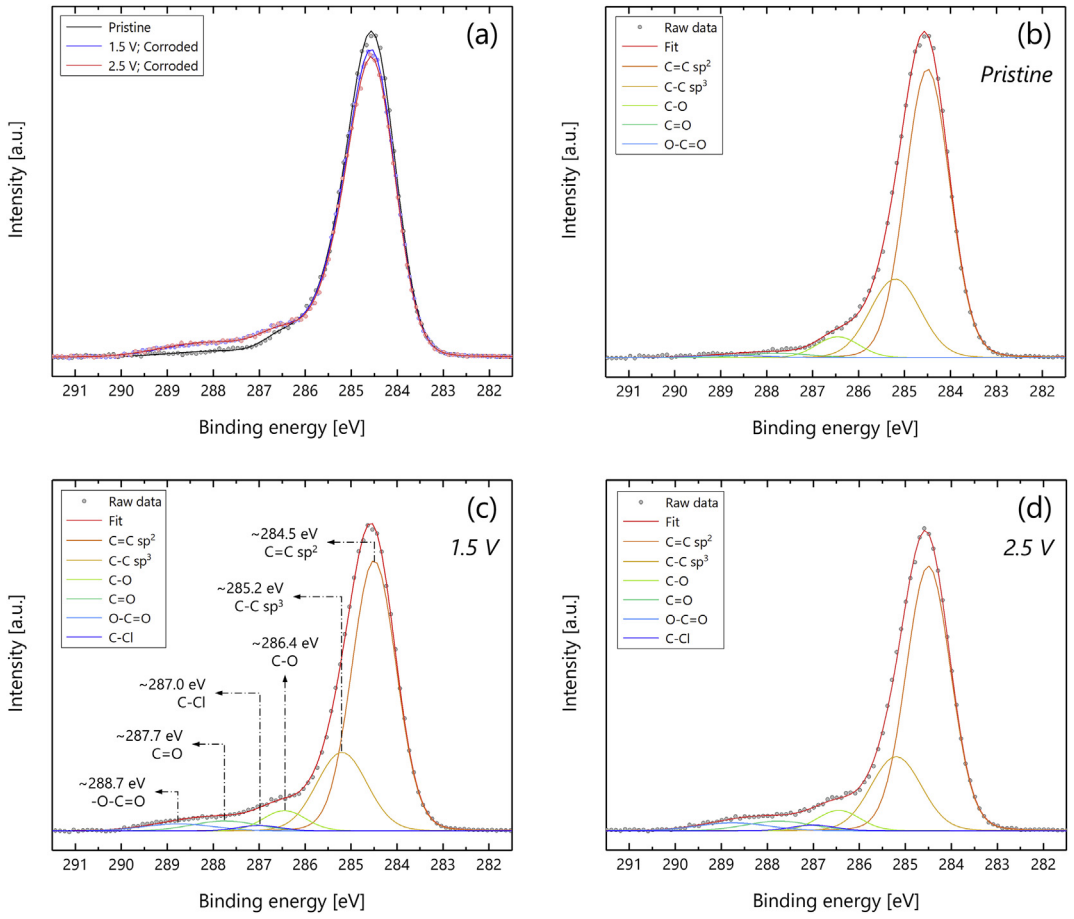

Fig. 5. High resolution carbon 1s XPS spectra of pristine and corroded a-C:H films: (a) comparison of pristine and corroded a-C:H. Deconvolution of: (b) pristine a-C:H; (c) a-C:H corroded at 1.5 V; (d) a-C:H corroded at 2.5 V. Binding energy position of the spectra calibrated to low-binding energy tail of C sp^2 peak at 284.5 eV (variation $\leq$ 70 meV). (A colour version of this figure can be viewed online.)

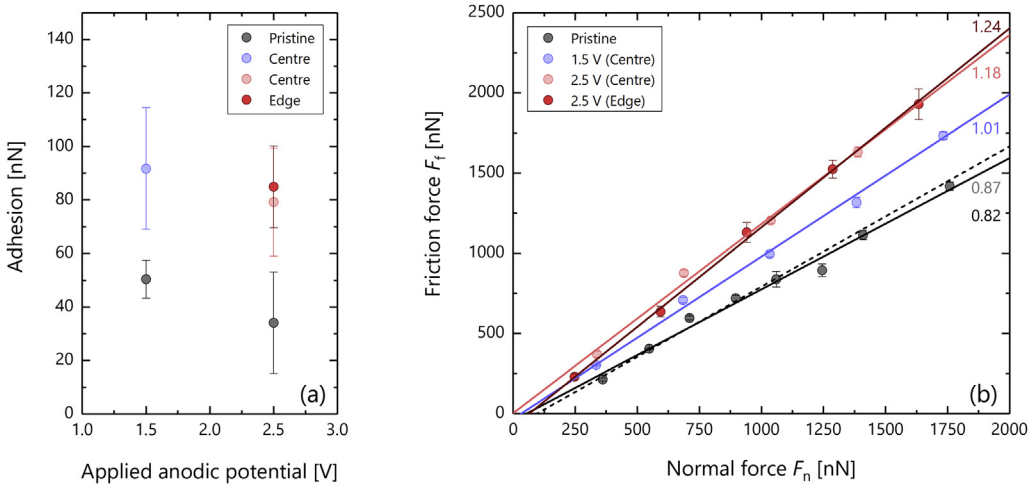

Fig. 6. Surface adhesion and friction response of a-C:H at various coating and corrosion locations (Fig. 1d) measured using a 'sharp' AFM probe: (a) surface adhesion values calculated from force-displacement measurements; (b) friction force as a function of normal force performed using lateral force microscopy (Fig. 1e), with the friction coefficient values reported adjacent to the corresponding linear fit. Solid black line fitted to data points corresponding to pristine sample corroded at 2.5 V; dashed black line fitted to data points corresponding to pristine sample corroded at 1.5 V. (A colour version of this figure can be viewed online.)

values. In order to interpret these differences, the prior findings in relation to (i) the a-C:H surface chemistry and (ii) the a-C:H topography are considered. In terms of (i) the a-C:H surface chemistry, corrosion at both anodic potentials has oxidised the a-C:H surface, forming a layer of oxidation products (alcohol, carbonyl and carboxyl groups). This will induce stronger attractive

interfacial interactions due to van der Waals interactions and H-bonding, and stronger capillary adhesion (as explained above) acting between the Si probe and the oxidised surface [28–32]. In addition, the oxidised layer is understood to be softer than the pristine a-C:H film [55], as the oxidation products disrupt the a-C:H network structure, thereby decreasing the film density. In terms of (ii) the a-C:H topography, only corrosion at 2.5 V has resulted in the a-C:H topography becoming more jagged at shorter length scales (decrease in exponent α). The RMS roughness (σ) is unlikely to factor in this instance, due to the comparable friction behaviour and yet different σ values of the two pristine coatings.

Thus, the increase in the measured friction force can be attributed to two features of the corroded a-C:H surface: (i) the surface chemistry and (ii) the surface topography. Feature (i) the surface oxidation, is considered responsible for the initial increase in friction seen between the pristine and corroded a-C:H films; and feature (ii) the jagged surface topography, is considered responsible for the additional increase in friction observed between the a-C:H films corroded at 1.5 V and 2.5 V. In order to explain these interpretations, several mechanisms are discussed below.

In adhesive friction the relation $F_f = \tau A_R$ applies, where τ is the shear strength at the contact interface and A_R is the real contact area, i.e. the exact area of contact between contacting roughness asperities. An increase in either A_R or τ or both, would increase the adhesive friction force. Considering the surface chemistry (i) in relation to the interfacial shear strength τ, the oxidised surface of a-C:H corroded at both anodic potentials will induce stronger attractive interfacial interactions (van der Waals interactions and H-bonding) between the Si probe and the oxidation products on the corroded a-C:H surface [28–32]. These heightened attractive intermolecular interactions at the contact interface, can contribute to an increased shear strength (resistance to sliding) at the boundary between the Si probe and the oxidised a-C:H surface, and thus an increase in the measured friction force. This hypothesis is also proposed by Li et al. [15] in relation to friction experiments carried out on oxidised a-C:H surfaces. Similarly, stronger capillary forces (driven by the Laplace pressure inside a capillary bridge), between the Si probe and oxidised (hydrophilic) surface of the corroded a-C:H film, can contribute to an increase in the interfacial shear strength and thus the measured increase in friction response, via increased attractive intermolecular interactions (H-bonding) at the probe-water-a-C:H interface [28–32]. Supporting the hypothesis for stronger attractive interfacial interactions occurring at the probe-corroded a-C:H interface is Fig. S5a, showing the raw data friction loops resulting from the first 100 nm sliding cycle of the 'sharp' Si probe over pristine and corroded a-C:H. It depicts a clear increase in the static friction (the linear component of the friction loop) for both corroded samples compared to the pristine a-C:H. An increase in the interfacial shear strength τ due to shearing *within* the materials at the interface (as opposed to shearing *at* the interface) is unlikely, because the layer of oxidation products formed on the corroded a-C:H surface will be softer than the pristine a-C:H (as discussed previously) [55], and would imply a potential decrease in τ rather than an increase.

If the surface chemistry (i) is now examined with regard to the influence it can have upon the area of real contact A_R, the softer oxidised surface of the a-C:H corroded at both anodic potentials would lead to an increase in A_R, as a result of LFM probe indentation. Indentation into a soft layer on the corroded a-C:H surface would imply that an additional deformation friction component - involving ploughing and displacement of the oxidised surface layer - would occur as the Si probe is slid over the a-C:H surface. Subsequent examination of the worn areas using AFM however, did not reveal any indication of ploughing tracks. Nevertheless, evidence for surface deformation and evolution of the interfacial contact area is present in Fig. S5a in the form of a 'friction strengthening' effect, where the friction force increases slightly with increasing scan distance [31]. This effect appears to develop over the 100 nm sliding distance and is more prominent for the corroded a-C:H.

If the surface topography (ii) of the corroded a-C:H is now considered with respect to the area of real contact A_R, an increase in this parameter is unlikely because, as mentioned previously, the ~10 nm radius of the sharp Si probe dominates the geometry of the contact interface. This is highlighted in Fig. S4, which shows the Hertzian contact diameter of the sharp probe (8 nm at a normal load of 1250 nN) scaled against a backdrop of the AFM micrographs for both pristine and corroded a-C:H surfaces. It illustrates that the spacing between the peaks and troughs of the 2.5 V corroded sample are small enough to fit the sharp probe. Thus at this scale, the area of contact between probe and surface should be unaffected by the roughness change.

However, in relation to the surface topography effect (ii), a further friction mechanism to consider is interlocking friction without deformation (ploughing) of asperities. Interlocking friction would occur if the probe "climbs" up roughness peaks but, due to internal friction within the contacting materials, does not fully recover the energy required to do this when descending into roughness valleys, resulting in a net energy loss. As mentioned previously, Fig. S4 shows that the spacing between the peaks and troughs of the 2.5 V corroded sample are small enough to fit the sharp probe, and to restrict its lateral movement; in contrast such artefacts are absent from the smooth topography of both the 1.5 V corroded sample and the pristine a-C:H. In addition to increasing the average friction force, such an interlocking mechanism can be expected to be reflected in an increase in the variation of the friction force signal, as the sharp probe slides across the rougher 2.5 V corroded a-C:H surface. Support for this hypothesis is reflected in the larger error bars present in the LFM data presented in Fig. 6b for the a-C:H corroded at 2.5 V, and Fig. S5a that shows the raw data friction loops resulting from the first 100 nm sliding cycle over pristine and corroded a-C:H. Fig. S5a depicts the saw-tooth modulation characteristic of stick-slip friction behaviour, which is particularly prominent in the data from the 2.5 V corroded a-C:H that also shows the highest friction force.

To provide further insights into the two features of the corroded a-C:H attributed to the increase in the measured friction force ((i) the surface oxidation and (ii) the jagged surface topography), a similar LFM study was performed, but utilising a 15 μm diameter silicon oxide colloidal probe. Unlike the outcome from the 'sharp' probe force-displacement measurements, no significant difference was seen between the pristine and corroded a-C:H in terms of its adhesion force (Fig. S6a). This is understood to be a probe geometry artefact and can be explained by the finite roughness on the surface of the colloidal probe, making it less sensitive to capillary adhesion than the sharp probe with its single point contact. The corroded a-C:H surfaces are again seen to generate higher friction forces than the pristine a-C:H (Fig. S6b), yet unlike the LFM study with the 'sharp' probe, no significant difference is observed between the response of the 2.5 V and 1.5 V corroded samples. Due to its size, the colloidal probe will not be influenced by the short length-scale topography variations of the 2.5 V corroded a-C:H film; for instance at a normal load of 200 nN, the Hertzian contact diameter of the 15 μm probe is 50 nm; so 'interlocking' between the probe and the surface will not occur. This is evident from Fig. S4 and the absence of the saw-tooth friction modulation behaviour in Fig. S5b. Therefore in the absence of surface topography effects, the increase in friction force measured for the corroded a-C:H surfaces in the colloidal probe tribological system is due only to (i) the surface chemistry. Stronger attractive interfacial interactions between the silicon oxide probe and the oxidation products on the corroded a-

C:H surface, although not clear from the adhesion force measurement (Fig. S6a), are evident in the form of the increased static friction component in the raw data friction loops shown in Fig. S5b. However, there is no evidence of the 'friction strengthening' effect [31], in Fig. S5b, suggesting that the colloidal probe did not deform the surface of the soft oxide layer on the corroded a-C:H and thus evolution of the interfacial contact area did not occur. The lower loading forces used and the larger geometry of the colloidal probe are two factors contributing to this result.

4. Conclusions

The influence of corrosion on the nanoscale topography and friction response of a hydrogenated amorphous carbon coating (a-C:H) was investigated. Two oxidative potentials (1.5 V and 2.5 V) were selected to corrode the samples for a total of 2.5 h utilising a 0.1 M KCl electrolyte. The a-C:H coating is found to corrode under these conditions at a rate of 26.4 nm h^{-1} at 2.5 V; and 0.5 nm h^{-1} at 1.5 V. Detailed analysis of AFM micrographs and subsequent utilisation of the height-height correlation function to completely characterise the surface by the extraction of roughness parameters, reveal that no changes are observed in the nanoscale topography of the a-C:H sample corroded at 1.5 V. However, the topography of the a-C:H film that underwent corrosion at 2.5 V changes significantly, becoming more jagged at shorter length scales, and displaying evidence of nanoscale surface material loss. XPS analysis shows that corrosion at both anodic potentials oxidises the a-C:H surface to a similar extent to form alcohol, carbonyl and carboxyl groups.

LFM and force-displacement measurements reveal that both the friction force and surface adhesion increases upon corrosion, with the a-C:H film corroded at 2.5 V exhibiting the highest friction coefficient. The outcome is attributed both to the changes in surface chemistry and the modified surface topography. The increased attractive interfacial interactions and capillary forces induced by the oxidation products on the surface of the corroded a-C:H, in addition to potential surface deformation and increased interfacial contact area between the sharp Si probe and the softer oxide layer, are regarded as responsible for the initial increase in friction seen between the pristine and corroded a-C:H films. An interlocking friction component resulting from the jagged surface topography, is considered to contribute to the additional increase in friction force observed between the a-C:H corroded at 1.5 V and 2.5 V when using a 'sharp' LFM probe.

CRediT authorship contribution statement

Fiona M. Elam: Conceptualization, Methodology, Validation, Formal analysis, Investigation, Writing – original draft, Writing – review & editing, Visualization. **Feng-Chun Hsia:** Methodology, Formal analysis, Investigation, Writing – review & editing. **Stefan van Vliet:** Formal analysis, Investigation, Writing – review & editing. **Roland Bliem:** Formal analysis, Writing – review & editing. **Liuquan Yang:** Resources, Writing – review & editing. **Bart Weber:** Writing – review & editing, Supervision, Funding acquisition. **Steve E. Franklin:** Conceptualization, Writing – review & editing, Supervision.

Declaration of competing interest

The authors declare that they have no known competing financial interests or personal relationships that could have appeared to influence the work reported in this paper.

Acknowledgements

This work has been carried out at the Advanced Research Centre for Nanolithography (ARCNL), a public-private partnership of the University of Amsterdam (UvA), the Vrije Universiteit Amsterdam (VU), the Netherlands Organisation for Scientific Research (NWO) and the semiconductor equipment manufacturer ASML. B.W. acknowledges funding from the NWO VENI grant No. VI.Veni.192.177.

Appendix A. Supplementary data

Supplementary data to this article can be found online at https://doi.org/10.1016/j.carbon.2021.04.068.

References

[1] A. Grill, Diamond-like carbon: state of the art, Diam. Relat. Mater. 8 (1999) 428–434, https://doi.org/10.1016/s0925-9635(98)00262-3.
[2] J. Robertson, Diamond-like amorphous carbon, Mater. Sci. Eng. R Rep. 37 (2002) 129–281, https://doi.org/10.1016/s0927-796x(02)00005-0.
[3] J. Robertson, Properties of diamond-like carbon, Surf. Coating. Technol. 50 (1992) 185–203, https://doi.org/10.1016/0257-8972(92)90001-Q.
[4] C. Donnet, A. Erdemir, Tribology of Diamond-like Carbon Films: Fundamentals and Applications, 2008, https://doi.org/10.1016/s1369-7021(08)70060-9.
[5] A. Grill, Diamond-like carbon coatings as biocompatible materials - an overview, Diam. Relat. Mater. 12 (2003) 166–170, https://doi.org/10.1016/S0925-9635(03)00018-9.
[6] A. Grill, Review of the tribology of diamond-like carbon, Wear 168 (1993) 143–153, https://doi.org/10.1016/0043-1648(93)90210-D.
[7] C. Casiraghi, J. Robertson, A.C. Ferrari, Diamond-like carbon for data and beer storage, Mater. Today 10 (2007) 44–53, https://doi.org/10.1016/S1369-7021(06)71791-6.
[8] J. Liu, X. Wang, B.J. Wu, T.F. Zhang, Y.X. Leng, N. Huang, Tribocorrosion behavior of DLC-coated CoCrMo alloy in simulated biological environment, Vacuum 92 (2013) 39–43, https://doi.org/10.1016/j.vacuum.2012.11.017.
[9] A. Hatem, J. Lin, R. Wei, R.D. Torres, C. Laurindo, P. Soares, Tribocorrosion behavior of DLC-coated Ti-6Al-4V alloy deposited by PIID and PEMS + PIID techniques for biomedical applications, Surf. Coating. Technol. 332 (2017) 223–232, https://doi.org/10.1016/j.surfcoat.2017.07.004.
[10] Q. Wang, F. Zhou, C. Wang, M.F. Yuen, M. Wang, T. Qian, M. Matsumoto, J. Yan, Comparison of tribological and electrochemical properties of TiN, CrN, TiAlN and a-C:H coatings in simulated body fluid, Mater. Chem. Phys. 158 (2015) 74–81, https://doi.org/10.1016/j.matchemphys.2015.03.039.
[11] C. Gou, L. Shang, Z. Lu, G. Zhang, S. Wang, Z. Wu, Probing the friction and wear behaviors of diamond-like carbon film in HCl and H2SO4 media, Mater. Res. Express 6 (2019) 106450, https://doi.org/10.1088/2053-1591/ab42fd.
[12] S.M.M. Oliveira, I.L.M. Barzotto, L. Vieira, A. Sene, P.A. Radi, S. Fraga, M.J. Bessa, J.P. Teixeira, I.C.S. Carvalho, N.S. da Silva, Tribocorrosion studies on diamond-like carbon film deposited by PECVD on 304 stainless steel in simulated body fluid, Biomed. Phys. Eng. Express 5 (2019), 045012, https://doi.org/10.1088/2057-1976/ab18e9.
[13] M. Cui, J. Pu, J. Liang, L. Wang, G. Zhang, Q. Xue, Corrosion and tribocorrosion performance of multilayer diamond-like carbon film in NaCl solution, RSC Adv. 5 (2015) 104829–104840, https://doi.org/10.1039/c5ra21207c.
[14] R. Bayón, A. Igartua, J.J. González, U. Ruiz de Gopegui, Influence of the carbon content on the corrosion and tribocorrosion performance of Ti-DLC coatings for biomedical alloys, Tribol. Int. 88 (2015) 115–125, https://doi.org/10.1016/j.triboint.2015.03.007.
[15] W. Li, D. He, W. Ren, L. Wang, L. Shang, G. Zhang, Tribological behaviors of DLC films in sulfuric acid and sodium hydroxide solutions, Surf. Interface Anal. 52 (2020) 396–406, https://doi.org/10.1002/sia.6747.
[16] F.R. Marciano, E.C. Almeida, D.A. Lima-Oliveira, E.J. Corat, V.J. Trava-Airoldi, Crystalline diamond particles into diamond-like carbon films: the influence of the particle sizes on the electrochemical corrosion resistance, Surf. Coating. Technol. 204 (2010) 2600–2604, https://doi.org/10.1016/j.surfcoat.2010.02.014.
[17] S. Tunmee, P. Photongkam, C. Euaruksakul, H. Takamatsu, X.L. Zhou, P. Wongpanya, K. Komatsu, K. Kanda, H. Ito, H. Saitoh, Investigation of pitting corrosion of diamond-like carbon films using synchrotron-based spectromicroscopy, J. Appl. Phys. 120 (2016) 195303, https://doi.org/10.1063/1.4967799.
[18] H.G. Kim, S.H. Ahn, J.G. Kim, S.J. Park, K.R. Lee, Corrosion performance of diamond-like carbon (DLC)-coated Ti alloy in the simulated body fluid environment, Diam. Relat. Mater. 14 (2005) 35–41, https://doi.org/10.1016/j.diamond.2004.06.034.
[19] Z.H. Liu, P. Lemoine, J.F. Zhao, D.M. Zhou, S. Mailley, E.T. McAdams, P. Maguire, J. McLaughlin, Characterisation of ultra-thin DLC coatings by SEM/EDX, AFM and electrochemical techniques, Diam. Relat. Mater. 7 (1998) 1059–1065, https://doi.org/10.1016/s0925-9635(98)00156-3.
[20] N. Moolsradoo, S. Watanabe, Influence of elements on the corrosion resistance

of DLC films, Adv. Mater. Sci. Eng. (2017) 3571454, https://doi.org/10.1155/2017/3571454.
[21] B.C. Ramos, E. Saito, V.J. Trava-Airoldi, A.O. Lobo, F.R. Marciano, Diamond-like carbon electrochemical corrosion resistance by addition of nanocrystalline diamond particles for biomedical applications, Surf. Coating. Technol. 259 (2014) 732–736, https://doi.org/10.1016/j.surfcoat.2014.09.066.
[22] M. Cui, J. Pu, G. Zhang, L. Wang, Q. Xue, The corrosion behaviors of multilayer diamond-like carbon coatings: influence of deposition periods and corrosive medium, RSC Adv. 6 (2016) 28570–28578, https://doi.org/10.1039/c6ra05527c.
[23] E.L. Dalibón, J.N. Pecina, M.N. Moscatelli, M.A. Ramírez Ramos, V.J. Trava-Airoldi, S.P. Brühl, Mechanical and corrosion behaviour of DLC and TiN coatings deposited on martensitic stainless steel, J. Bio Tribo Corrosion 5 (2019) 34, https://doi.org/10.1007/s40735-019-0228-6.
[24] P.D. Maguire, J.A. McLaughlin, T.I.T. Okpalugo, P. Lemoine, P. Papakonstantinou, E.T. McAdams, M. Needham, A.A. Ogwu, M. Ball, G.A. Abbas, Mechanical stability, corrosion performance and bioresponse of amorphous diamond-like carbon for medical stents and guidewires, Diam. Relat. Mater. 14 (2005) 1277–1288, https://doi.org/10.1016/j.diamond.2004.12.023.
[25] E.L. Dalibón, L. Escalada, S. Simison, C. Forsich, D. Heim, S.P. Brühl, Mechanical and corrosion behavior of thick and soft DLC coatings, Surf. Coating. Technol. 312 (2017) 101–109, https://doi.org/10.1016/j.surfcoat.2016.10.006.
[26] E. Liu, H.W. Kwek, Electrochemical performance of diamond-like carbon thin films, Thin Solid Films 516 (2008) 5201–5205, https://doi.org/10.1016/j.tsf.2007.07.089.
[27] O. Sharifahmadian, F. Mahboubi, S. Yazdani, Comparison between corrosion behaviour of DLC and N-DLC coatings deposited by DC-pulsed PACVD technique, Diam. Relat. Mater. 95 (2019) 60–70, https://doi.org/10.1016/j.diamond.2019.04.007.
[28] C. Donnet, Recent progress on the tribology of doped diamond-like and carbon alloy coatings: a review, Surf. Coating. Technol. 100–101 (1998) 180–186, https://doi.org/10.1016/S0257-8972(97)00611-7.
[29] C. Donnet, A. Grill, Friction control of diamond-like carbon coatings, Surf. Coating. Technol. 94–95 (1997) 456–462, https://doi.org/10.1016/S0257-8972(97)00275-2.
[30] H. Li, T. Xu, C. Wang, J. Chen, H. Zhou, H. Liu, Friction-induced physical and chemical interactions among diamond-like carbon film, steel ball and water and/or oxygen molecules, Diam. Relat. Mater. 15 (2006) 1228–1234, https://doi.org/10.1016/j.diamond.2005.09.038.
[31] X. Zeng, Y. Peng, M. Yu, H. Lang, X. Cao, K. Zou, Dynamic sliding enhancement on the friction and adhesion of graphene, graphene oxide, and fluorinated graphene, ACS Appl. Mater. Interfaces 10 (2018) 8214–8224, https://doi.org/10.1021/acsami.7b19518.
[32] X. Zeng, Y. Peng, H. Lang, L. Liu, Controllable nanotribological properties of graphene nanosheets, Sci. Rep. 7 (2017) 41891, https://doi.org/10.1038/srep41891.
[33] S.J. McMaster, T.W. Liskiewicz, A. Neville, B.D. Beake, Probing fatigue resistance in multi-layer DLC coatings by micro- and nano-impact: correlation to erosion tests, Surf. Coating. Technol. 402 (2020) 126319, https://doi.org/10.1016/j.surfcoat.2020.126319.
[34] Sean Michael Carley, Diamond-like Carbon Coatings for Improved Mechanical Performance of Polymer Materials, The University of Leeds, 2017. http://etheses.whiterose.ac.uk/id/eprint/18406.
[35] J. Kim, J. Lee, Y. Tak, Relationship between carbon corrosion and positive electrode potential in a proton-exchange membrane fuel cell during start/stop operation, J. Power Sources 192 (2009) 674–678, https://doi.org/10.1016/j.jpowsour.2009.03.039.
[36] D. Necas, P. Klapetek, Gwyddion: an open-source software for SPM data analysis, Cent. Eur. J. Phys. 10 (2012) 181–188, https://doi.org/10.2478/s11534-011-0096-2.
[37] M. Varenberg, I. Etsion, G. Halperin, An improved wedge calibration method for lateral force in atomic force microscopy, Rev. Sci. Instrum. 74 (2003) 3362–3367, https://doi.org/10.1063/1.1584082.
[38] D. Vorselen, E.S. Kooreman, G.J.L. Wuite, W.H. Roos, Controlled tip wear on high roughness surfaces yields gradual broadening and rounding of cantilever tips, Sci. Rep. 6 (2016) 36972, https://doi.org/10.1038/srep36972.
[39] Z. Ahmad, Principles of Corrosion Engineering and Corrosion Control, first ed., Elsevier Ltd, Oxford, England, 2006 https://doi.org/10.1016/B978-0-7506-5924-6.X5000-4.
[40] H.S. Zhang, J.L. Endrino, A. Anders, Comparative surface and nano-tribological characteristics of nanocomposite diamond-like carbon thin films doped by silver, Appl. Surf. Sci. 255 (2008) 2551–2556, https://doi.org/10.1016/j.apsusc.2008.07.193.
[41] E.V. Zavedeev, B. Jaeggi, J. Zuercher, B. Neuenschwander, O.S. Zilova, M.L. Shupegin, M.Y. Presniakov, S.M. Pimenov, Effects of AFM tip wear on frictional images of laser-patterned diamond-like nanocomposite films, Wear (2018) 416–417, https://doi.org/10.1016/j.wear.2018.09.008, 1–5.
[42] Y.P. Zhao, H.N. Yang, G.C. Wang, T.M. Lu, Extraction of real-space correlation function of a rough surface by light scattering using diode array detectors, Appl. Phys. Lett. 68 (1995) 3063–3065, https://doi.org/10.1063/1.116423.
[43] H.N. Yang, Y.P. Zhao, G.C. Wang, T.M. Lu, Noise-induced roughening evolution of amorphous si films grown by thermal evaporation, Phys. Rev. Lett. 76 (1996) 3774–3777, https://doi.org/10.1103/PhysRevLett.76.3774.
[44] J. Krim, J.O. Indekeu, Roughness exponents: a paradox resolved, Phys. Rev. E 48 (1993) 1576–1578, https://doi.org/10.1103/PhysRevE.48.1576.
[45] J. Filik, P.W. May, S.R.J. Pearce, R.K. Wild, K.R. Hallam, XPS and laser Raman analysis of hydrogenated amorphous carbon films, Diam. Relat. Mater. 12 (2003) 974–978, https://doi.org/10.1016/S0925-9635(02)00374-6.
[46] Y. Zhang, C. Guerra-Nuñez, M. Li, J. Michler, H.G. Park, M.D. Rossell, R. Erni, I. Utke, High conformity and large domain monocrystalline anatase on multiwall carbon nanotube core-shell nanostructure: synthesis, structure, and interface, Chem. Mater. 28 (2016) 3488–3496, https://doi.org/10.1021/acs.chemmater.6b01209.
[47] A.A. Al-Azizi, O. Eryilmaz, A. Erdemir, S.H. Kim, Surface structure of hydrogenated diamond-like carbon: origin of run-in behavior prior to superlubricious interfacial shear, Langmuir 31 (2015) 1711–1721, https://doi.org/10.1021/la504612c.
[48] M. Pourbaix, Atlas of Chemical and Electrochemical Equilibria in Aqueous Solutions, second ed., National Association of Corrosion Engineers, Houston, Texas, 1974. https://doi.org/10.4028/www.scientific.net/msf.251-254.143.
[49] N. Macauley, D.D. Papadias, J. Fairweather, D. Spernjak, D. Langlois, R. Ahluwalia, K.L. More, R. Mukundan, R.L. Borup, Carbon corrosion in PEM fuel cells and the development of accelerated stress tests, J. Electrochem. Soc. 165 (2018) F3148–F3160, https://doi.org/10.1149/2.0061806jes.
[50] Y. Yin, L. Hang, J. Xu, D.R. McKenzie, M.M.M. Bilek, Surface adsorption and wetting properties of amorphous diamond-like carbon thin films for biomedical applications, Thin Solid Films 516 (2008) 5157–5161, https://doi.org/10.1016/j.tsf.2007.07.012.
[51] Z. Wei, Y.P. Zhao, Growth of liquid bridge in AFM, J. Phys. D Appl. Phys. 40 (2007) 4368–4375, https://doi.org/10.1088/0022-3727/40/14/036.
[52] T. Stifter, O. Marti, B. Bhushan, Theoretical investigation of the distance dependence of capillary and van der Waals forces in scanning force microscopy, Phys. Rev. B 62 (2000) 13667–13673, https://doi.org/10.1103/PhysRevB.62.13667.
[53] E. Hsiao, M.J. Marino, S.H. Kim, Effects of gas adsorption isotherm and liquid contact angle on capillary force for sphere-on-flat and cone-on-flat geometries, J. Colloid Interface Sci. 352 (2010) 549–557, https://doi.org/10.1016/j.jcis.2010.09.005.
[54] P.J. van Zwol, G. Palasantzas, J.T.M. De Hosson, Influence of roughness on capillary forces between hydrophilic surfaces, Phys. Rev. E 78 (2008), 031606, https://doi.org/10.1103/PhysRevE.78.031606.
[55] D.Y. Wang, C.L. Chang, W.Y. Ho, Oxidation behavior of diamond-like carbon films, Surf. Coating. Technol. 120–121 (1999) 138–144, https://doi.org/10.1016/S0257-8972(99)00350-3.